Journal of Magnetic Resonance 278 (2017) 51–59

Contents lists available at ScienceDirect

Journal of Magnetic Resonance

journal homepage: www.elsevier.com/locate/jmr

Communication

Oval gradient coils for an open magnetic resonance imaging system with a vertical magnetic field

Koki Matsuzawa [a], Mitsushi Abe [b], Katsumi Kose [a], Yasuhiko Terada [a,*]

[a] Institute of Applied Physics, University of Tsukuba, Tsukuba, Ibaraki 305-8573, Japan
[b] Applied Energy Systems Research Department Center for Technology Innovation, Hitachi, Ltd., Hitachi, Japan

ARTICLE INFO

Article history:
Received 15 December 2016
Revised 6 March 2017
Accepted 18 March 2017
Available online 20 March 2017

Keywords:
Oval gradient coil
Open MRI
Vertical-field MRI
Truncated singular value decomposition

ABSTRACT

Existing open magnetic resonance imaging (MRI) systems use biplanar gradient coils for the spatial encoding of signals. We propose using novel oval gradient coils for an open vertical-field MRI. We designed oval gradients for a 0.3 T open MRI system and showed that such a system could outperform a traditional biplanar gradient system while maintaining adequate gradient homogeneity and subject accessibility. Such oval gradient coils would exhibit high efficiency, low inductance and resistance, and high switching capability. Although the designed oval Y and Z coils showed more heat dissipation and less cooling capability than biplanar coils with the same gap, they showed an efficient heat-dissipation path to the surrounding air, which would alleviate the heat problem. The performance of the designed oval-coil system was demonstrated experimentally by imaging a human hand.

1. Introduction

There are two types of magnetic resonance imaging (MRI) systems; namely, closed MRI and open MRI. Open MRI uses a vertical-field magnet with an open space between the two opposing magnetic poles. Compared with closed MRI, an open MRI offers adequate performance while being more comfortable, less claustrophobic, and more convenient for patients. Recently, open low-field MRI scanners for extremities have become popular, mainly because these modalities are maintenance-free, more comfortable for patients, and more accessible than high-field scanners [1–4].

Gradient coils are key components of MRI systems, being used to generate linearly varying magnetic fields that spatially encode the imaging region. In modern MRI applications, there are increasing demands for strong gradient fields and fast switching of coil currents to enable rapid image acquisition with high image quality. It follows that the primary criteria for gradient coil design should include high efficiency and linearity with short switching times (i.e., low inductance). At the same time, secondary concerns such as eddy current induction and thermal heating due to gradient switching should not be overlooked. Therefore, gradient coil design is not straightforward and many design methods have been proposed to optimize the design criteria while balancing the various trade-offs for particular applications [5–7].

An open MRI system uses a pair of planar coils, referred to as biplanar gradient coils [8], that are attached to the two opposing magnetic poles. An advantage of the biplanar gradient geometry is that it offers a maximized open space in the magnet gap (i.e., the greatest accessibility for the patient). However, coil parameters such as gradient efficiency, inductance, and resistance depend on the size of the coil, with small coils leading to good performance. Therefore, it is desirable to design coils to be as small as possible [6]. Because the imaging volume is typically assumed to be within a sphere or an ellipsoid, from a performance perspective, it is desirable that the coil shape is also spherical or ellipsoidal. Practically, because of the accessibility constraint, the direction along the sample or subject needs to be open, and a cylindrical or oval shape could be a better choice. Imaging human hands is one of the typical applications of an open MRI system, and its imaging volume is set to be ellipsoidal according to the shape of the hand. In this paper, we propose oval gradients for human hand imaging that have the potential to maximize coil performance, but have not yet been applied in an open MRI system. Oval coils offer better coverage of the imaging volume than biplanar coils with the same gap size; therefore, they might have superior performance.

A key technology for designing oval gradients is the combination of matrix-inversion optimization techniques with discrete representations of the current surface [9–15]. This approach enables the design of arbitrarily shaped gradient coils, such as ultrashort coils, head gradient coils with highly asymmetric geometry, and shoulder-slotted gradient coils [13]. One promising

* Corresponding author.
E-mail address: terada@bk.tsukuba.ac.jp (Y. Terada).

http://dx.doi.org/10.1016/j.jmr.2017.03.009
1090-7807/

approach to matrix-inversion optimization is the use of truncated singular value decomposition (TSVD). Its major advantage is that magnetic field accuracies can be controlled by choosing an appropriate number of eigenmodes that make major contributions to the magnetic field. This concept has been demonstrated recently in the context of biplanar coils [11,14,15].

In this paper, we design oval gradient coils for a 0.3 T open MRI system used for hand imaging [16]. We compare the coil performance with biplanar gradient coils having the same gap size. We also construct the designed oval gradient coils and demonstrate their usefulness.

2. Methods

The gradient coils were designed using the TSVD method [11,14,15]. In brief, the current surface of each gradient coil was discretized into a mesh of triangles. The stream function T_i for the current density at each node (i.e., the current potential) was then solved by matrix inversion using TSVD and Tikhonov regularization [17].

The magnetic field at a point j was expressed as,

$$B_j = \Sigma_i A_{i,j} T_i.$$

Here the coefficient $A_{i,j}$ was calculated using the Biot–Savart law. Defining $B = (B_1, \ldots, B_n)^T$ and $T = (T_1, \ldots, T_m)^T$, this equation was reformulated as a matrix multiplication $B = AT$. The matrix A can be written using TSVD and given by

$$A = U \Lambda V^T,$$

where U and V are unitary matrices, and Λ is a diagonal matrix containing the singular values $\lambda_i, \mathrm{i} = 1, \ldots, \min(\mathrm{n}, \mathrm{m})$. Using the columns of U, denoted $u_1, \ldots, u_n$, and those of V, denoted $v_1, \ldots, v_m$

$$A = \Sigma_i \lambda_i u_i v_i^T.$$

The current potential matrix T is then calculated as

$$T = A^{-1} B = \Sigma_i \frac{v_i u_i^T}{\lambda_i} B.$$

A rank-k approximation of T can be given by a truncated sum of rank-one matrices; namely,

$$T^{(k)} = \Sigma_i^k \frac{v_i u_i^T}{\lambda_i} B.$$

The eigenmodes with large λ make the dominant contributions to the magnetic field, and the field accuracy can be controlled by choosing an appropriate number of those eigenmodes manually.

A discrete wire path was obtained for the coil design by contouring the current potential distribution over the mesh elements. Then a Biot–Savart-law calculation was performed to obtain the magnetic field strength per unit current at the target points $B_z^{BS}(\mathbf{r})$. This result was used to calculate the gradient efficiency η, defined as the field gradient strength at the origin per unit current, and other parameters of the coil. The accuracy of the gradient field was measured by the nonlinearity of the field gradient, $\max \left| \frac{G(\boldsymbol{r})}{G(0)} - 1 \right|$, where $G(\boldsymbol{r})$ is the field gradient strength per unit current at position $\boldsymbol{r}$. The gradient field accuracy was also evaluated by the gradient homogeneity, δ, defined as $\frac{1}{V} \int (B_z^{BS}(\boldsymbol{r})/B_0(\boldsymbol{r}) - 1)^2 d\boldsymbol{r}$, where $B_0(\boldsymbol{r})$ is the desired field at position $\boldsymbol{r}$, and the integral is taken over the target area for a volume V. The inductance L was calculated according to an approximated curve integral [18] similar to the Neumann formula: $L = \frac{\mu_0}{4\pi} \left(\oint \frac{d\boldsymbol{l}_1 \cdot d\boldsymbol{l}_2}{\Delta} \right)_{\Delta > a/2} + \frac{\mu_0}{4\pi} lY + O(\mu_0 a)$, where $d\boldsymbol{l}_1$ and $d\boldsymbol{l}_2$ are two elementary filaments separated by the distance Δ, a is the radius of the wire, l is the length of the wire, Y is the constant depending on the distribution of the current in the cross section of the wire, and $Y = 0$ when the current inside the wire is neglected. The error $O(\mu_0 a)$ is small when $l \gg a$. For simplicity, we neglected the second and third terms.

The figure of merit (FOMs) [5,7] that characterize the coil performance irrespective of the number of turns of wire N can be given by $\eta^2/L\sqrt{\delta}$ or η^2/L, η^2/R (similar to $\eta/\sqrt{R}$), and ηw, where R is the resistance, and w is the minimum wire spacing. These three FOMs are indicators of coil performance representing rapid gradient switching ($\eta^2/L\sqrt{\delta}$), less heat dissipation (η^2/R), and high cooling capability (ηw), respectively [7]. The resistance R depends on the cross section of the wire. Because the FOM η^2/R is independent of N for a fixed layer thickness (see [19] and references therein), we calculated R assuming a flat strip line with the fixed thickness of 1 mm and the width of w.

Oval X, Y, and Z gradients were designed for an extremity-dedicated open MRI system [16] with a field strength of 0.3 T, a magnet gap of 120 mm, and pole-piece diameter of 360 mm. The target region for the gradient field was set as an ellipsoidal volume ($100 \times 100 \times 50\ \mathrm{mm}^3$) at the center of the magnet field. The geometry of the gradient coils was an oval cylinder (see Table 1 and Fig. 1(a)). The x- and z-axes corresponded to the major and minor directions of the oval plane. The y-axis corresponded to the cylinder axis. The magnetic field was parallel to the z-axis. For comparison, we designed biplanar gradients with the same gap size as the height of the oval gradients using TSVD.

To improve the TSVD solution, we assigned a weight to each node T_i to mitigate distance variations [14,15]. This corresponds to making a variable transformation $T_i \rightarrow T_i/\delta_i$, where δ_i is the weight assigned to the ith node. Here, we used $\delta_i = \sqrt{x_i^2 + y_i^2}$, where (x_i, y_i, z_i) are the Cartesian coordinates of the ith node. Without using the weighing factor, the current potential contours tend to have more complicated shapes near the center area than at the edge area, which could cause problems for large magnetic energy, large resistive energy, and complicated patterns. The reason for this complexity is discussed in the following. In the original TSVD method, low-ordered eigenmodes with large λ are preferentially selected. The low-ordered modes tend to have centered current potential distribution [14], because the finite elements located near the target imaging volume could generate large magnetic fields.

TSVD solutions depend on the initial pattern, which is often empirically determined. Here we used initial patterns given by the following equations (Fig. 1(b)–(d)) to obtain a smoother solution [14,15].

$$T_{0,x}(r,\theta) = T_{c,x} \times \cos\theta \times \sin\left\{ \frac{\pi}{2} \left(1 - \frac{r - R_c}{|r - R_c|} \cdot \frac{2r - R_c}{R_c} \right) \right\},$$

$$T_{0,y}(r,\theta) = T_{c,y} \times \sin\theta \times \sin\left\{ \frac{\pi}{2} \left(1 - \frac{r - R_c}{|r - R_c|} \cdot \frac{2r - R_c}{R_c} \right) \right\},$$

Table 1
Coil dimensions and parameters for TSVD calculations.

	X	Y	Z
Coil dimensions			
Width [major axis x] (mm)	158	160	162
Height [minor axis z] (mm)	108	110	112
Length [cylindrical axis y] (mm)	200	200	200
Parameters for TSVD			
Tikhonov regularization factor	N/A	N/A	5×10^{-7}
Number of selected eigenmodes	16	43	16
Number of current nodes	8192	8192	8192
Nonlinearity constraint (%)	8	8	8

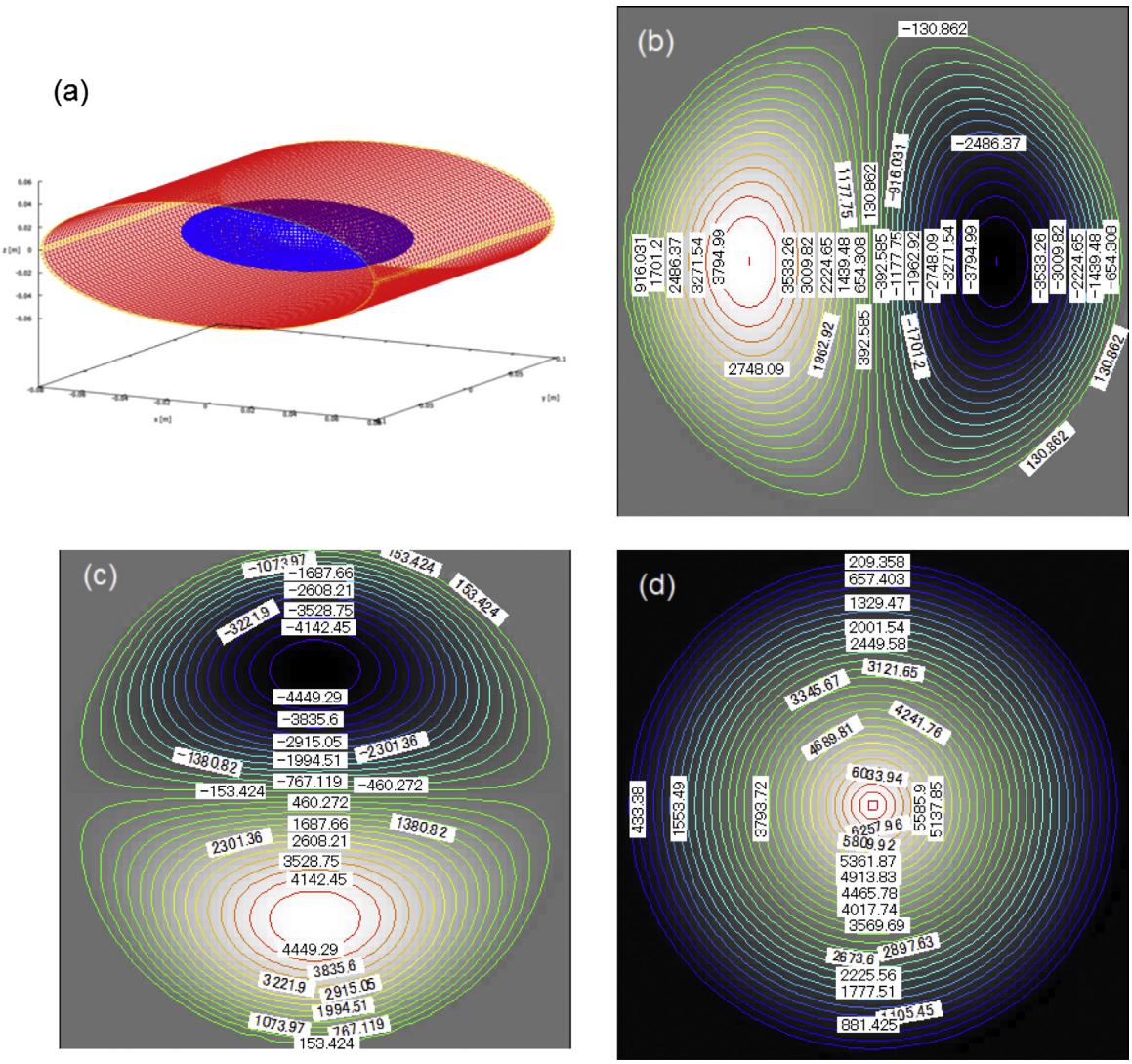

Fig. 1. (a) Mesh of the oval cylinder plane used for coil design. (b)–(d) Initial distribution and contours of current potential used for the TSVD calculation: (b) X-gradient, (c) Y-gradient, and (d) Z-gradient.

$$T_{0,z}(r,\theta) = T_{c,z} \times \frac{r}{R_c}.$$

Here $T_{0,x}, T_{0,y}$, and $T_{0,z}$ are the initial current potentials for the X, Y, and Z coils, respectively. r and θ are the polar coordinates in the coil plane, and R_c is the radius of the coil plane. $T_{c,x}$, $T_{c,y}$, and $T_{c,z}$ are constants that were determined manually, such that the initial magnetic field was closer to the target magnetic field. Here, these constants were 203 (oval X), 238 (oval Y), 343 (oval Z), 384 (biplanar X), 384 (biplanar Y), and 490 (biplanar Z).

The gradient design algorithm and graphical user interface were implemented in C# and .NET Framework 4.5 with the Math.NET Numerics library. The parameters used for TSVD are summarized in Table 1. The computation time for TSVD was approximately 3 min for each coil using a 4 GHz CPU (Intel Core™ i7-4790K) with 32 GB of RAM.

Coils for the designed oval gradients were constructed by winding polyethylene-coated copper wire (0.5 mm in diameter) and fixing to plastic plates (0.1 mm thick) using epoxy resin. The X, Y, and Z coil elements were stacked and fixed on an acrylic cylinder (4 mm thick).

The MRI system was equipped with a radiofrequency (RF) coil, the constructed gradient-coil set, an MRI digital transceiver (DTRX-6, MRTechnology, Tsukuba, Japan), a transmitter, a three-channel gradient driver (10 A, 30 V, DST Inc., Asaka, Japan), and a temperature control system. The RF coil was an oval-cylinder solenoid coil (100 mm × 50 mm aperture, 220 mm long) shielded with brass plates (0.5 mm thick) and a 5-mm-thick aluminum plate.

The gradient efficiency of the built coil was measured using a regularly spaced three-dimensional (3D) lattice phantom (Fig. 2) made of acrylic square trenches filled with baby oil. The lattice phantom was imaged using a 3D spin echo sequence. Then, the distance in the readout direction in pixel n_x, between two vertex points was measured from the image. The efficiency η in the readout direction was calculated as

$$\eta = \frac{2\pi n_x}{\gamma L T_x I},$$

where γ is the gyromagnetic ratio, L is the geometric distance between the two vertex points, T_x is the readout time, and I is the current flowing through the gradient coil. For the demonstration, the left hand of a healthy volunteer was imaged using the oval-gradient system. The pulse sequence used was a 3D gradient echo with a varying echo time TE. Imaging parameters were set as follows: repetition time = 40 ms, field of view = 100 mm × 150 mm × 50 mm, matrix size = 256 × 192 × 32, flip angle = 45°, and number

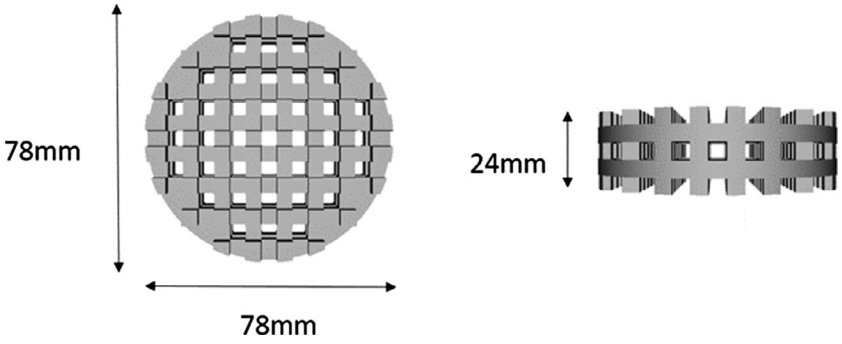

Fig. 2. Schematic of three-dimensional lattice phantom.

of excitations = 2. The bandwidths were 125 kHz (TE = 2 ms), 100 kHz (TE = 6 ms), and 25 kHz (TE = 11 ms).

3. Results and discussion

Fig. 3(a) shows the dependence of the efficiency η on the number of the current-potential contours N, with the efficiency increasing linearly with N. The oval X and Z coils had higher efficiency values than the corresponding biplanar X and Z coils for a given N, reflecting the closed geometry of the oval coils. The Y coil had a comparable efficiency for both geometries. This is because the oval coil was not closed in the y direction. The values of the FOMs for the oval and biplanar coils (see Fig. 3(b)-(d)) were almost independent of N but were dependent on the coil geometry and therefore represent good measures of the coil performance. The mean $\eta^2/L\sqrt{\delta}$ over N (see Fig. 3(e)) for the oval X, Y, and Z coils were 2.28, 1.24, and 2.74 times higher than those for the biplanar X, Y, and Z coils, respectively. This indicates that the oval gradients systematically outperformed the biplanar gradients in terms of gradient-switching speed.

The mean η^2/R for the oval X coil was larger than that for the biplanar X coil (Fig. 3(f)). However, the oval Y and Z coils had a lower mean η^2/R than the biplanar Y and Z coils. The mean ηw also showed the same tendency (Fig. 3(g)). These values indicated that the oval Y and Z coils had lower performance than biplanar ones in terms of heat dissipation and cooling capability. This is caused by the fact that the area of the oval coil planes was smaller than that of the biplanar coils; therefore, the minimum wire spacing w became smaller for a given N. This led to a narrower wire width and a larger resistance for the oval Y and Z coils, resulting in more heat dissipation and less cooling capability than for the biplanar coils.

However, it is worth noting that the coil surfaces for the oval gradients were exposed to the air, enabling efficient cooling paths. In addition, the oval coils were not directly attached close to the pole pieces, in contrast to traditional biplanar gradient coils, which are attached close to the pole pieces. The heat in biplanar coils may accumulate in the space between the gradient coil and the pole pieces, often resulting in thermal drift by the magnet and consequent image artifacts such as blurring. To rectify this, a water-cooling system might be necessary for biplanar coils. For oval-gradient coils, the inherent efficient cooling by the surrounding air avoids this problem altogether and would alleviate the larger heat generation for the Y and Z coils.

Table 2 summarizes the detailed theoretical properties of the oval and biplanar gradients for N = 60 (X), 50 (Y), and 40 (Z). Each oval coil exhibited high efficiency and low inductance, in comparison with the corresponding biplanar coil, while maintaining a comparable accuracy for the gradient field. As described before, the oval Y and Z coils had higher resistance. Fig. 4 shows the winding patterns. Unlike the biplanar coils, the oval coils had asymmetric geometry with respect to the z-axis, which led to asymmetric winding patterns for X and Y. Fig. 5 shows the construction and installation of the designed oval-gradient coils. Here we used the 0.5 mm-diameter wire, which was slightly larger than the minimum wire spacing w for the Y (0.357 mm) and Z (0.425 mm) coils, to reduce the coil resistance down to the practical level. For example, if we construct the Y coil using a round wire with the diameter w, the coil resistance would reach to 5.4 Ω, which could pass only 5.6 A current with the gradient amplifier used in this study (maximum current = 10 A and voltage = 30 V). Thus, we used the wider 0.5 mm diameter wire, which had the theoretical resistance of 2.8 Ω and could pass the maximum current of 10 A. Because we used the larger diameter wire, the winding patterns of the constructed Y and Z coils were different from those of the designed coils, and part of the wires were densely wound. However, most parts were constructed as designed, and the deviated part was located close to the edge of the coil planes, which contributed less to the gradient field in the imaging volume. Moreover, the difference in the wire spacing was <0.2 mm, which was as small as the manufacturing error.

Table 3 compares the performance of the theoretical and constructed coils. Here, we used the theoretical value of w for the constructed X coil. The Y and Z coils were partly densely wound, and thus we assumed w to be a double of the cladding thickness of the wires, which resulted in small values of ηw. The efficiency values (in mT/m/A) of the constructed coils were 8.0 (X), 4.5 (Y), and 6.7 (Z), respectively. These values were slightly higher than the theoretical ones, possibly because of the effect of mirror currents flowing in the pole pieces. To estimate the mirror current effect, we used a simple model of mirror-current planes (Fig. 6(a)). Then the enhancement effect caused by the mirror current can be modeled as follows:

$$\boldsymbol{J}_{\text{total}} = I\delta(\boldsymbol{r}_{\text{w}}) + \beta(I\delta(\boldsymbol{r}_u) + I\delta(\boldsymbol{r}_l)),$$

where $\boldsymbol{J}_{\text{total}}$ is the total current density considering mirror current, $\boldsymbol{r}_{\text{w}}$ is the position of the wire path in the coil plane, $\boldsymbol{r}_u$ and $\boldsymbol{r}_l$ are the corresponding mirror positions in the upper and lower pole pieces, respectively. β is the relative amplitude of the mirror current. Fig. 6(b) shows the x-z plane of the 3D image of the lattice phantom. The light blue points in the figure are the theoretical positions of the vertex points calculated with the theoretical η and without considering mirror current ($\beta = 0$). The theoretical points correspond to the imaged vertex points of the phantom near the center of the image, but deviate at large z. The red points in Fig. 6 (b) were the theoretical vertex positions assuming that $\beta = 0.3$, and showed a good agreement with the imaged vertex positions. There is a small difference between the theoretical and imaged positions near the edge (at large x), possibly because we assumed semi-infinite mirror-current planes and neglected the finite size.

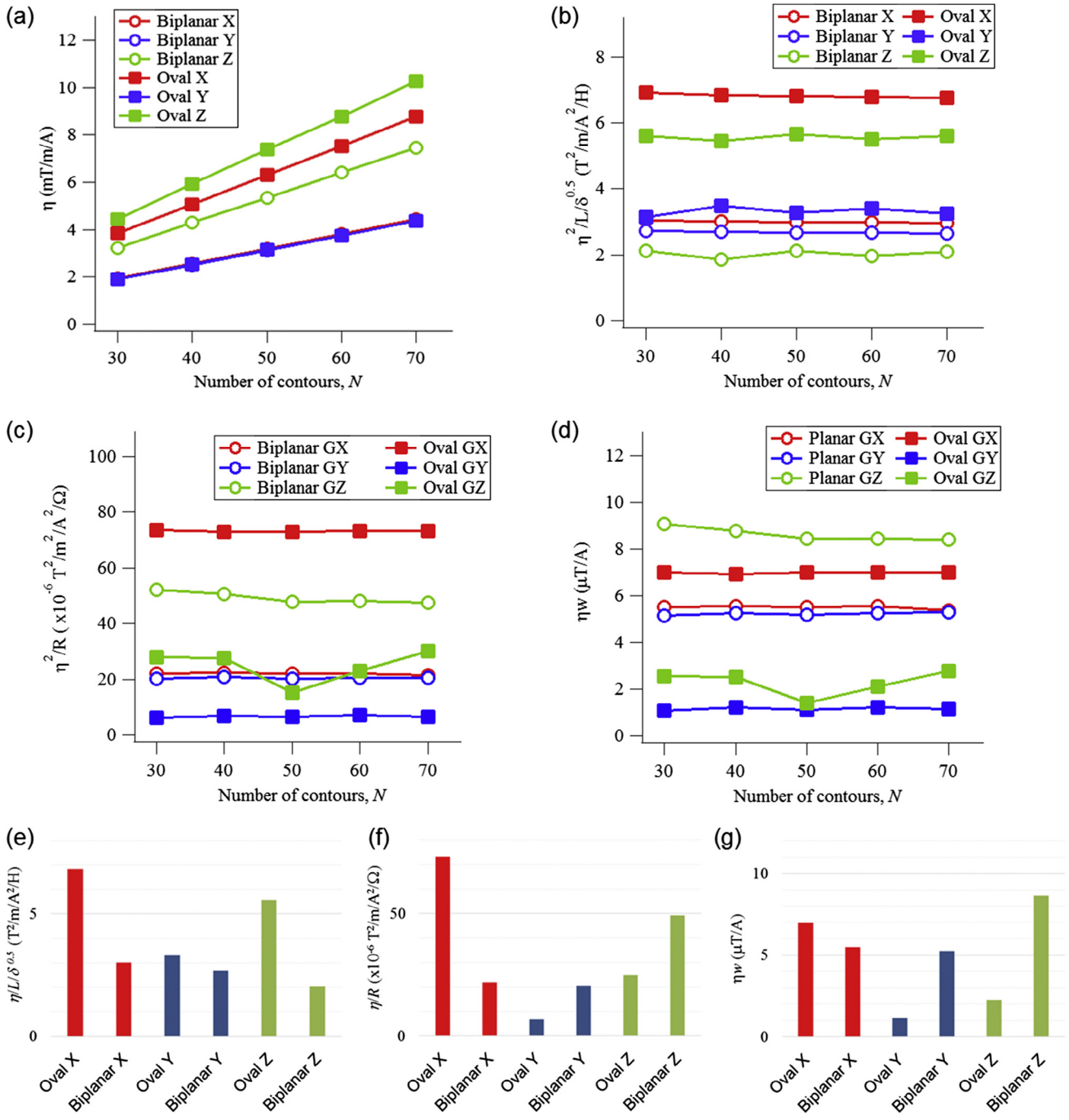

Fig. 3. (a)–(d) Dependence of coil performance on the number of contours N: (a) efficiency η, (b) $\eta^2/L\sqrt{\delta}$, (c) η^2/R, and (d) ηw. (d)–(g) Mean FOMs over N: (e) $\eta^2/L\sqrt{\delta}$, (f) η^2/R, and (g) ηw.

These results indicated that the mirror-current effect enhanced the gradient efficiency, in particular near the z-axis, but distorted the gradient linearity. To correct the gradient distortion, the design method that considers the mirror-current effect might be required. For the biplanar gradients, in contrast, the coil planes are parallel to the pole surfaces, and gradient distortion would hardly appear even with mirror current.

Despite the closed geometry, the oval gradient coils could be closely fitted to the RF coil, and the whole system retained high accessibility by the subject or sample.

High efficiency and consequent high-gradient amplitudes provide great benefits for imaging. For example, a signal can be acquired with a wide bandwidth and a short sampling time. This allows imaging with a short TE, giving the potential merits of high signal-to-noise ratio and additional image contrast of tissues with a short transverse relaxation time T_2. Fig. 7 shows the different image contrasts for the volunteer's left hand for different TEs. As the TE increases, the cartilage (indicated by white arrows in the coronal images), which has a longer T_2 than other tissues [20], is imaged more brightly, whereas the tendon (indicated by white arrows in the axial images) with its shorter T_2 [21] was imaged less brightly. The signal-loss artifact (circled in the axial image) appeared when TE = 11 ms. Such artifacts in gradient-echo images are the result of field inhomogeneity and

Table 2
Theoretical performance of the oval and biplanar coils. The resistance R was calculated assuming the copper strip line with the thickness of 1 mm and the width of w.

Type	Oval coils			Biplanar coils		
	X	Y	Z	X	Y	Z
Number of contours N	60	50	40	60	50	40
Efficiency η (mT/m/A)	7.54	3.14	5.92	3.80	3.13	4.30
Nonlinearity (%)	8.42	8.55	8.27	8.04	8.25	8.13
Gradient homogeneity δ (%)	0.0401	0.0201	0.0651	0.00787	0.00921	0.0799
Min. wire spacing w (mm)	0.928	0.357	0.425	1.46	1.66	2.04
Inductance L (μH)	419	211	252	546	381	351
Resistance R (Ω)	0.777	1.53	1.27	0.654	0.482	0.364
FOM, $\eta^2/L\sqrt{\delta}$ ($T^2/m^2/A^2/H$)	6.79	3.28	5.44	2.98	2.67	1.86
FOM, η^2/R ($\mu T^2/m^2/A^2/\Omega$)	73.2	6.45	27.6	22.1	20.3	50.7
FOM, ηw (μT/A)	7.00	1.12	2.52	5.54	5.19	8.77

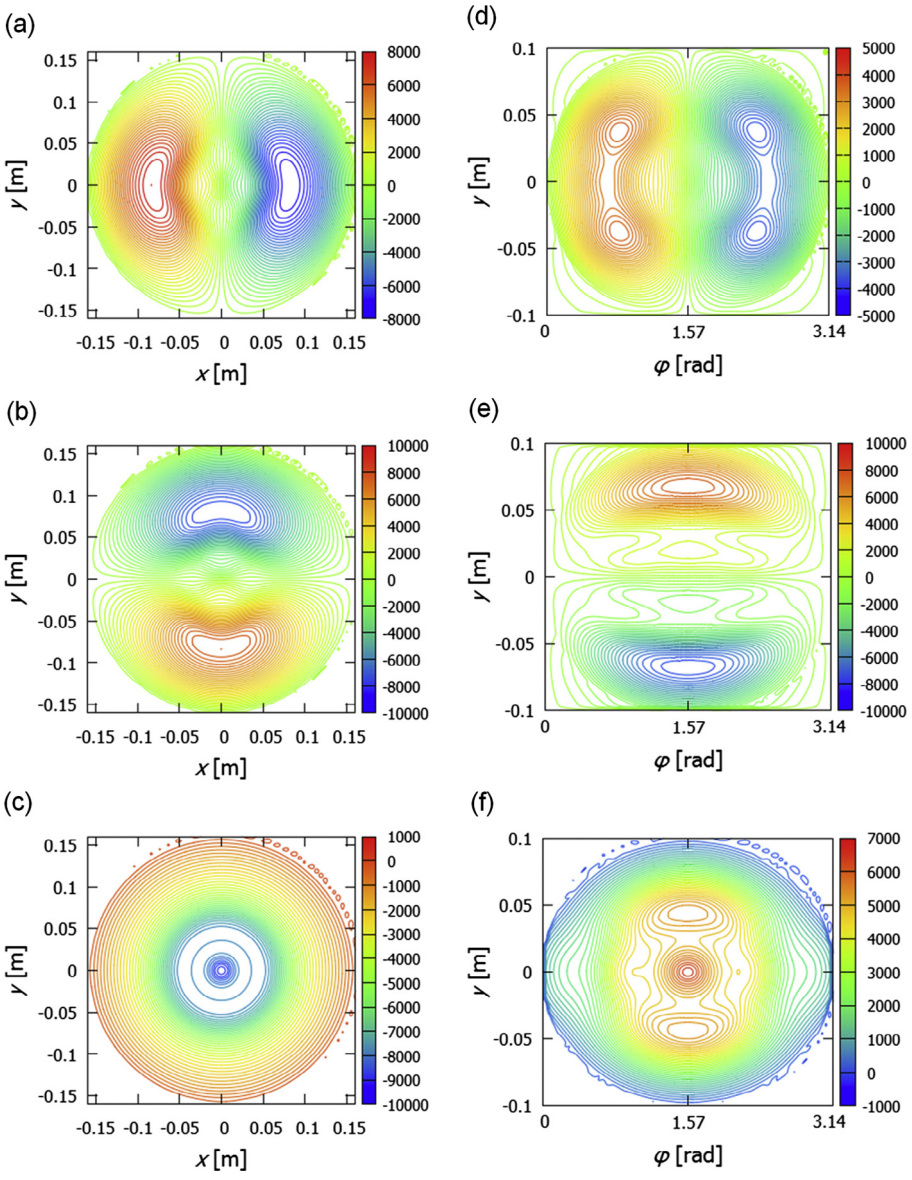

Fig. 4. Winding patterns for various gradients: (a) biplanar X, (b) biplanar Y, and (c) biplanar Z, (d) oval X, (e) oval Y, and (f) oval Z. For the oval patterns, the parametric equations of the coil path line with respect to the parameter φ are given by $x(\varphi) = a\cos\varphi$ and $z(\varphi) = b\sin\varphi$, where a and b are the semi-major and semi-minor axes of the oval plane, respectively.

become less noticeable as the TE decreased. It is worth noting that imaging with a short TE (TE = 2 ms) was possible only for the oval gradients. This was not possible for the biplanar gradients and the existing gradient amplifier, because of the limited maximum gradient strength.

The short sampling time also allows imaging with a large matrix for a given TE, which is essential for magnetic resonance microscopy [22] (i.e., imaging with a microscopic resolution). A strong gradient is also indispensable for ultrafast imaging modalities such as echo planar imaging [23,24].

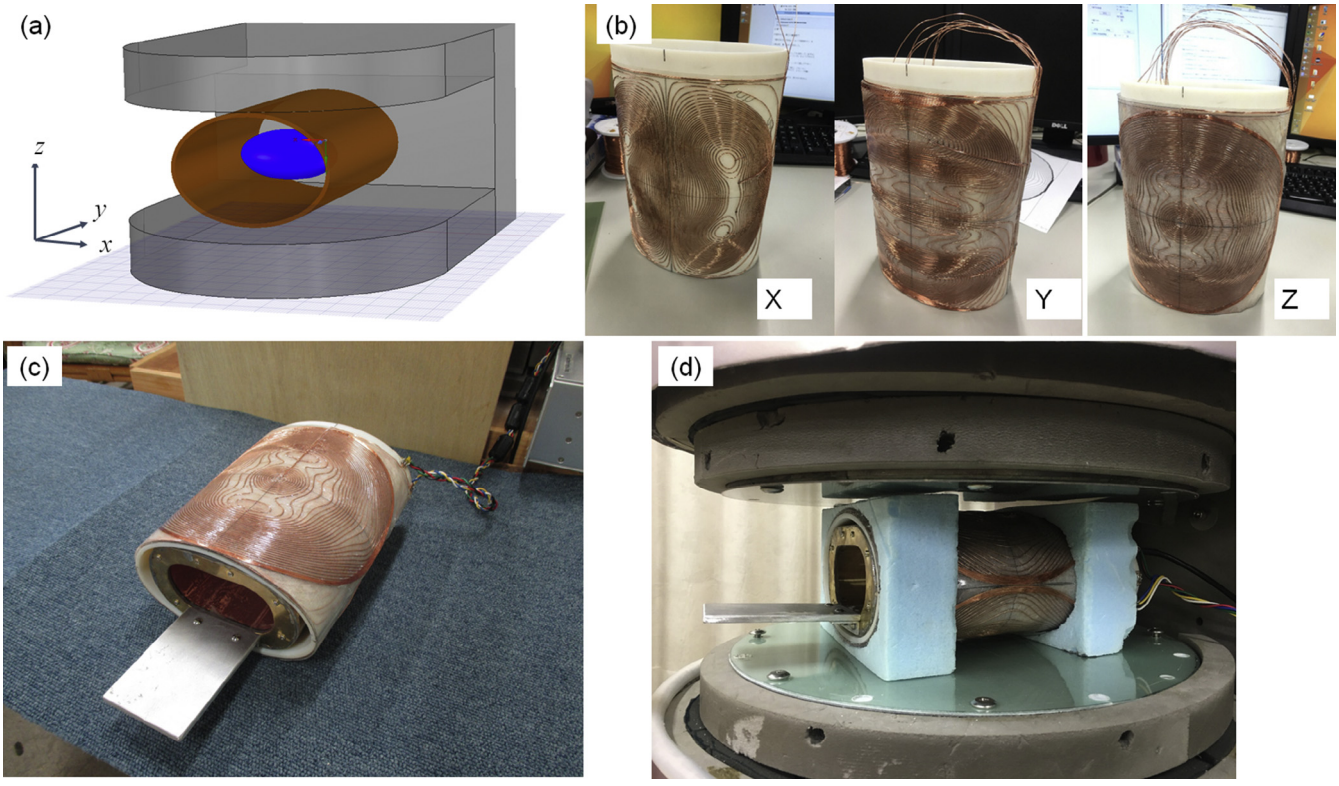

Fig. 5. (a) Schematic of oval gradients (colored in brown), target area (colored in blue), and a C-type magnet. (b) Construction process for the designed oval gradient coils: after the X coil is fixed to the plate, the Y coil is stacked on it, and finally the Z coil. (c) The oval gradient coils and the RF probe. (d) Installation of the gradient coils and the RF probe. (For interpretation of the references to color in this figure legend, the reader is referred to the web version of this article.)

Table 3
Performance of the theoretical and constructed coils. The resistance R was calculated assuming the round copper wire with the diameter of 0.5 mm.

Type	Theoretical coils			Constructed coils		
	X	Y	Z	X	Y	Z
Efficiency η (mT/m/A)	7.54	3.14	5.92	8.0	4.5	6.7
Inductance L (μH)	419	211	252	474	343	299
Resistance R (Ω)	3.67	2.77	2.75	3.95	3.58	3.09
FOM, η^2/L ($T^2/m^2/A^2/H$)	0.135	0.0466	0.139	0.14	0.060	0.15
FOM, η^2/R ($\mu T^2/m^2/A^2/\Omega$)	15.5	3.55	12.7	16	5.7	14
FOM, ηw (μT/A)	7.00	1.12	2.52	7.4	0.095	0.14

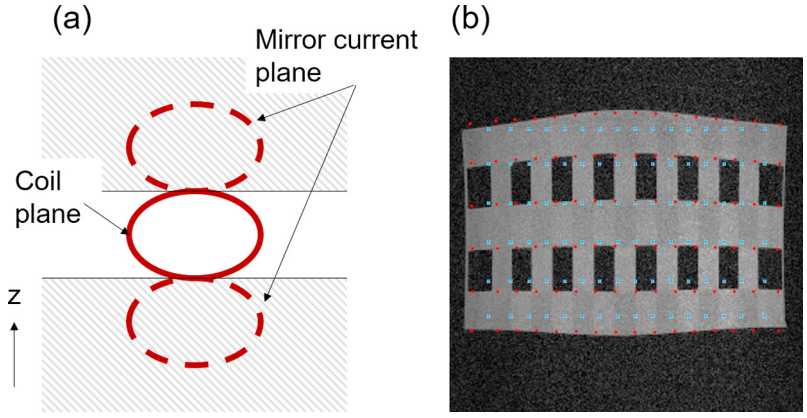

Fig. 6. (a) Mirror current model. (b) x–z image of a regularly spaced 3D lattice phantom. The light blue points indicate the vertex positions calculated without considering mirror current. The red points indicate the vertex positions calculated with mirror current. (For interpretation of the references to color in this figure legend, the reader is referred to the web version of this article.)

For the proof-of-principle implementation that we have described, the gradient field was not shielded, which may cause undesired secondary fields generated by eddy currents. Although this was not severe for the standard sequences used in this study, faster and stronger switching of the gradient coils might lead to image artifacts originating in a strong eddy-current field. With the

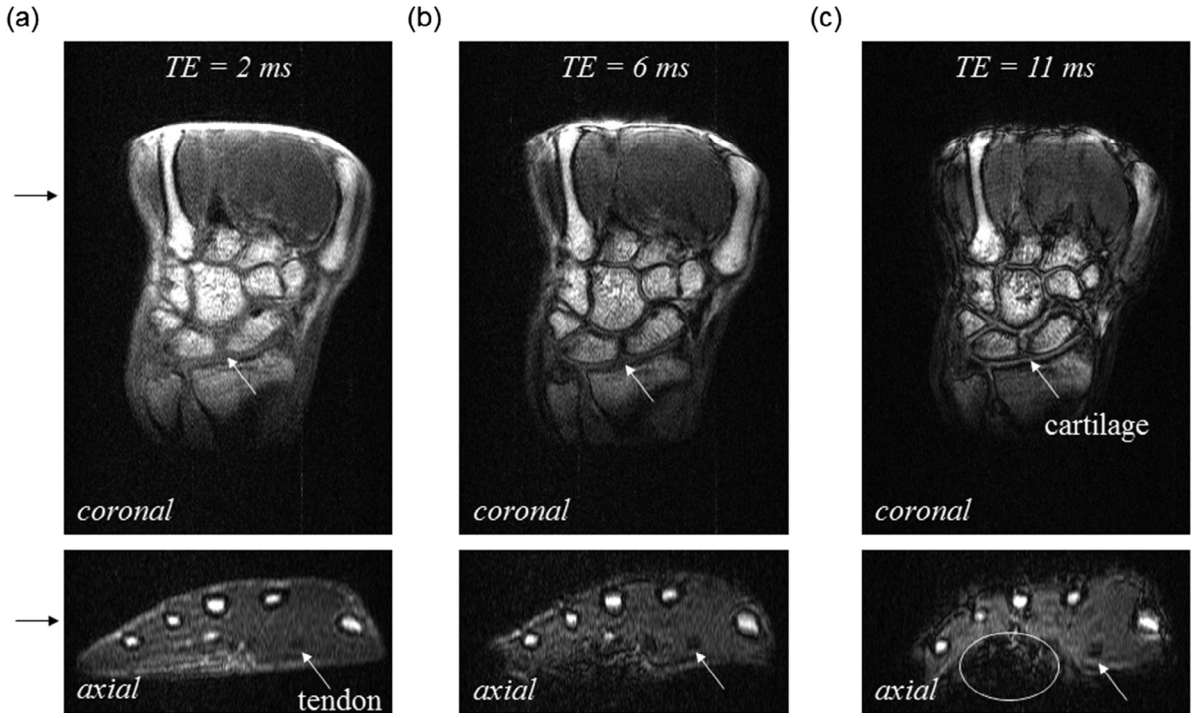

Fig. 7. 3D-GRE MR images of the left hand of a healthy volunteer: (a) TE = 2 ms, (b) TE = 6 ms, and (c) TE = 11 ms. The black arrows pointing to the coronal and axial images indicate the slice positions of the axial and coronal images. The white arrows in the coronal images indicate the cartilage. The white arrows in the axial images indicate the tendon. The white circle indicates a signal-loss artifact.

current design framework, however, the implementation of a shielded coil would not be difficult. A combination of an oval main coil and a biplanar shielded coil might represent a better solution for maintaining high accessibility and openness in the magnetic gap.

4. Conclusion

In conclusion, we have proposed using oval gradients for a vertical-field MRI system. The oval gradients could maintain adequate gradient homogeneity, openness, and high subject accessibility. The oval gradients were found to have a much higher switching capability than traditional biplanar gradients with the same gap. The oval Y and Z coils had lower performance than biplanar coils in terms of heat dissipation and cooling capability. However, the oval coils offered an efficient heat-dissipation path to the surrounding air, which would alleviate the heat problem. The merits of their high efficiency were demonstrated by short-TE imaging of a human hand. We concluded that oval gradients could outperform traditional biplanar gradients.

Acknowledgement

The authors would like to acknowledge Mr. Jyupei Matsuzaki for his assistance with the imaging experiments.

References

[1] G. Verhoek, M. Zanetti, S. Duewell, H. Zollinger, J. Hodler, MRI of the foot and ankle: diagnostic performance and patient acceptance of a dedicated low field MR scanner, J. Magn. Reson. Imaging 8 (1998) 711–716.
[2] S. Ghazinoor, H.V. Crues III, C. Crowley, Low-field musculoskeletal MRI, J. Magn. Reson. Imaging 25 (2007) 234–244.
[3] T. Suzuki, S. Ito, S. Handa, K. Kose, Y. Okamoto, M. Miami, M. Sugihara, M. Horikoshi, H. Tsuboi, T. Hayashi, D. Goto, I. Matsumoto, T. Sumida, New low-field extremity MRI, compacTscan: comparison with whole-body 1.5 T conventional MRI, Mod. Rheumatol. 20 (2010) 331–336.
[4] S.B. Cohen, H. Potter, A. Deodhar, P. Emery, P. Conaghan, M. Ostergaard, Extremity magnetic resonance imaging in rheumatoid arthritis: updated literature review, Arthritis Care Res. 63 (2011) 660–665.
[5] R. Turner, Gradient coil design: a review of methods, Magn. Reson. Imaging 11 (1993) 903–920.
[6] S.S. Hidalgo-Tobon, Theory of gradient coil design methods for magnetic resonance imaging, Concepts Magn. Reson. A 36 (2010) 223–242.
[7] M.S. Poole, P.T. While, H.S. Lopez, S. Crozier, Minimax current density gradient coils: analysis of coil performance and heating, Mang. Reson. Med. 68 (2012) 639–648.
[8] M.A. Martens, L.S. Petropoulos, R.W. Brown, J.H. Andrews, M.A. Morich, J.L. Patrick, Insertable biplanar gradient coils for magnetic resonance imaging, Rev. Sci. Instrum. 62 (1991) 2639.
[9] S. Pissanetzky, Minimum energy MRI gradient coils of general geometry, Meas. Sci. Technol. 3 (1992) 667–673.
[10] G.N. Peeren, Stream function approach for determining optimal surface currents, J. Comput. Phys. 191 (2003) 305–321.
[11] M. Abe, T. Nakayama, S. Okamura, K. Matsuoka, A new technique to optimize the coil winding path for the arbitrarily distributed magnetic field and application to a helical confinement system, Phys. Plasmas 10 (2003) 1022–1033.
[12] R. Lemdiasov, R. Ludwig, A stream function method for gradient coil design, Concepts Magn. Reson. B 26 (2005) 67–80.
[13] M. Poole, R. Bowtell, Novel gradient coils designed using a boundary element method, Concepts Magn. Reson. B 31 (2007) 162–175.
[14] M. Abe, A design tool for magnetic resonance imaging gradient coils using DUCAS with weighted nodes and initial current potentials, IEEE Trans. Magn. 49 (2013) 5645.
[15] M. Abe, A design technique of MRI active shield gradient coil using node current potentials and triangular finite elements, IEEE Trans. Magn. 50 (2014) 5100911.
[16] Y. Terada, S. Kono, T. Uchiumi, K. Kose, R. Miyagi, E. Yamabe, Y. Fujinaga, H. Yoshioka, Improved reliability in skeletal age assessment using a pediatric hand MR scanner with a 0.3T permanent magnet, Magn. Reson. Med. Sci. 13 (2014) 215–219.
[17] A. Neumaier, Solving ill-conditioned and singular linear systems: a tutorial on regularization, Siam Rev. 40 (1998) 636–666.
[18] R. Dengler, Self inductance of a wire loop as a curve integral, Adv. Electromagn. 5 (2016) 1–8.
[19] M. Poole, H.S. Lopez, S. Crozier, Adaptively regularised gradient coils for reduced local heating, Concepts Magn. Reson. B: Magn. Reson. Eng. 33 (2008) 220–227.
[20] H.E. Smith, T.J. Mosher, B.J. Dardzinski, B.G. Collins, Q.X. Yang, V.J. Schmithorst, M.B. Smith, Spatial variation in cartilage T2 of the knee, J. Magn. Reson. Imaging 14 (2001) 50–55.

[21] M.D. Robson, P.D. Gatehouse, M. Bydder, G.M. Bydder, Magnetic resonance: an introduction to ultrashort TE (UTE) imaging, J. Comput. Assist. Tomogr. 27 (2003) 825–846.
[22] P.T. Callaghan, Principles of Nuclear Magnetic Resonance Microscopy, Oxford University Press Inc., New York, 1991.
[23] P. Mansfield, Multi-planar image formation using NMR spin echoes, J. Phys. C: Solid State Phys. 10 (1977) L55–L58.
[24] A.C. Silva, H. Merkle, Hardware considerations for functional magnetic resonance imaging, Concepts Magn. Reson. A 16 (2003) 35–49.